ACS APPLIED MATERIALS & INTERFACES

Research Article

www.acsami.org

Highly Conductive Diamond–Graphite Nanohybrid Films with Enhanced Electron Field Emission and Microplasma Illumination Properties

Adhimoorthy Saravanan,[†] Bohr-Ran Huang,[†] Kamatchi Jothiramalingam Sankaran, [‡,§] Nyan-Hwa Tai, [‡] and I-Nan Lin*[,∥]

[†]Graduate Institute of Electro-Optical Engineering and Department of Electronic Engineering, National TaiwanUniversity of Science and Technology, Taipei 106,Taiwan Republic of China

[‡]Department of Materials Science and Engineering, National Tsing Hua University, Hsinchu 300, Taiwan Republic of China

[§]Institute for Materials Research (IMO), Hasselt University, 3590 Diepenbeek, Belgium

[∥]Department of Physics, Tamkang University, Tamsui 251, Taiwan Republic of China

ABSTRACT: Bias-enhanced nucleation and growth of diamond–graphite nanohybrid (DGH) films on silicon substrates by microwave plasma enhanced chemical vapor deposition using CH_4/N_2 gas mixture is reported herein. It is observed that by controlling the growth time, the microstructure of the DGH films and, thus, the electrical conductivity and the electron field emission (EFE) properties of the films can be manipulated. The films grown for 30 min (DGH_{B30}) possess needle-like geometry, which comprised of a diamond core encased in a sheath of sp^2-bonded graphitic phase. These films achieved high conductivity of σ = 900 S/cm and superior EFE properties, namely, low turn-on field of 2.9 V/μm and high EFE current density of 3.8 mA/cm^2 at an applied field of 6.0 V/μm. On increasing the growth time to 60 min (the DGH_{B60}), the acicular grain growth ceased and formed nanographite clusters or defective diamond clusters (n-diamond). Even though DGH_{B60} films possess higher electrical conductivity (σ = 1549 S/cm) than the DGH_{B30} films, the EFE properties degraded. The implication of this result is that higher conductivity by itself does not guarantee better EFE properties. The nanosized diamond grains with needle-like geometry are the most promising ones for the electron emission, exclusively when they are encased in graphene-like layers. The salient feature of such materials with unique granular structure is that their conductivity and EFE properties can be tuned in a wide range, which makes them especially useful in practical applications.

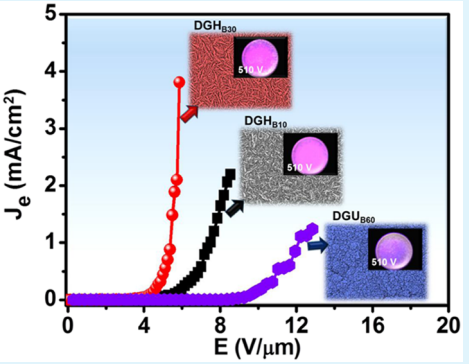

KEYWORDS: *diamond–graphite nanohybrid films, negative bias, electron field emission, growth time, microstructure, microplasma illumination*

1. INTRODUCTION

Carbon-based materials are noble and require low voltages for electron field emission (EFE). A wide range of carbon materials, such as carbon nanotubes, graphene, and diamond-like carbon films have been extensively studied for the development of electron field emitters. Carbon-based field emitters with low threshold field can provide sufficiently high EFE current densities for use in flat panel displays, X-rays and microplasma applications.[1−5] However, long-term emission stability and low emission density are the major issues for most of the carbon-based EFE devices. On the other hand, the diamond films possess strong covalent bonds with excellent physical and chemical properties and therefore exhibits the highest reliability.[6,7] Diamond-film-based EFE devices have been used in the fabrication of flat panel displays and microelectronic devices.[8−10] Ultrananocrystalline diamond (UNCD) film grown in CH_4/Ar plasma is a special form of diamond film that contains ultrasmall (2−5 nm) sp^3-bonded diamond grains with amorphous carbon (a-C) grain boundaries of considerable thickness, and hence, it possesses superior conductivity and enhanced EFE properties as compared to other kinds of diamond films.[11] However, the UNCD films are still not as conductive as the carbon-based films due to low conductivity of the a-C phases present in the grain boundaries of UNCD films that limits the EFE properties of the films.[12−14]

Incorporation of nitrogen in the CH_4/Ar plasma demonstrated enormous improvement in electrical conductivity and EFE properties.[15,16] The conductivity of UNCD films has been increased to 143 S/cm. Gruen et al. grew diamond films with needle-like grains, achieving higher conductivity.[17] Later, it was observed that the high conductivity of such films arise from the presence of graphitic phase encasing the needle-like diamond grains.[18,19] Post-treatment of these needle-like granular structured diamond films in hydrogen plasma for 10 min has

Received: April 13, 2015
Accepted: June 9, 2015
Published: June 9, 2015

DOI: 10.1021/acsami.5b03166
ACS Appl. Mater. Interfaces 2015, 7, 14035−14042

further increased the conductivity up to 216 S/cm.[20] Incorporation of N into diamond films via the addition of N_2 into reacting gas requires high growth temperature (800 °C). Bias enhanced nucleation and growth (BEN−BEG) processes have been utilized to induce the formation of graphitic phase in microcrystalline diamond (MCD),[21] nanocrystalline diamond,[22] and UNCD[23] films at low growth temperature (<500 °C). Enhanced EFE properties for these films have been attained.[21−23] The BEN−BEG processes have great potential for inducing the formation of nanographitic phase in diamond films. This is also a promising method for preparing the highly conducting diamond films without the need for high growth temperature.

In this study, diamond-graphite nanohybrid (DGH) films were grown in CH_4/N_2 plasma with the application of negative biased voltage (−250 V). Highly conductive DGH films were obtained at low substrate temperature. It has been observed that the microstructure of thus obtained DGH films change markedly with the growth time, as do the conductivity and the EFE properties of the films. The DGH films grown for 30 min exhibit the best EFE properties with lowest turn-on field of 2.9 V/μm, whereas the films grown for 60 min have the highest conductivity (σ = 1549 S/cm) but slightly degraded EFE properties. The conductivity and EFE properties of the DGH films are closely correlated with the microstructure of the films. The evolution of microstructure with the thickness of the films were systematically investigated using transmission electron microscopy, and the formation mechanism for the change in microstructure was discussed based on TEM observations.

2. EXPERIMENTAL METHODS

The DGH films were grown on *n*-type silicon substrates by microwave plasma enhanced chemical vapor deposition system. Prior to the deposition of DGH films, the silicon substrates were seeded by ultrasonication in a methanol solution containing nanosized diamond powders (~5 nm) and Ti powders (~32.5 nm) for 45 min.[24] The substrates were ultrasonicated again in methanol for 1 min to eradicate the possibly adhered nanoparticles. The DGH films were grown in CH_4(6%)/N_2(94%) plasma and excited by a 1200 W microwave power with a 50 Torr total pressure. A negative bias voltage (−250 V) was applied to the Si substrate when the pressure reached 50 Torr in the growth period of 10−60 min. The corresponding films were designated as DGH_{BT}, where T is the growth time. In addition, the DGH films were also grown without bias for 30 min to facilitate the comparison and the corresponding films were designated as DGH_{N30}. The species contained in the plasma during film's deposition process were analyzed using in situ optical emission spectroscopy (OES, BWTEK). The morphology and the bonding structure of the films were characterized using scanning electron microscopy (SEM; Jeol JSM-6500F) and visible-Raman spectroscopy (λ: 632.8 nm, Lab Raman HR800, JobinYvon), respectively. The local microstructure and bonding structure of the samples were examined using TEM (Jeol 2100F) and electron energy loss spectroscopy (EELS; GatanEnfina), respectively.

The EFE properties of the DGH films were measured with a tunable parallel plate setup using Cu-rod (3 mm in diameter) as anode, in which the cathode-to-anode distance was controlled using a micrometer. The current−voltage (I−V) characteristics were measured using an electrometer (Keithley 2410) under pressure below 10^{-6} Torr. The EFE parameters were extracted from the obtained I−V curves by using the Fowler−Nordheim (F−N) model.[25] The turn-on field (E_0) was designated as the point of interception of the straight lines extrapolated from the low- and high-field segments of the F−N plots, namely, ln (J_e/E^2) versus 1/E plots, where J_e is the EFE current density and E is the applied field. The electrical conductivity measurements of the DGH films were carried out by Hall measurements in van der Pauw configuration (ECOPIA HMS-3000). The plasma illumination (PI) characteristics of the microcavity were investigated systematically. In the microcavity, indium tin oxide (ITO)-coated glass was used as anode and the DGH films were used as cathode. The cathode-to-anode separation was fixed by a polytetrafluoroethylene (PTFE) spacer (1.0 mm in thickness). A circular hole about 3.0 mm in diameter was cut out from the PTFE spacer to form a microcavity. The plasma was triggered using a pulsed direct current voltage in a bipolar pulse mode (20 ms square pulse, 6 kHz repetition rate). The chamber was evacuated to reach a base pressure of 0.1 mTorr and then purged with Ar for 10 min up to 2 Torr. The Ar gas was channeled into the chamber at a flow rate of 10 sccm throughout the measurements. The plasma current versus applied voltage characteristics was measured using an electrometer (Keithley 237).

3. RESULTS

3.1. Material Characterization. The OES spectrum of the CH_4/N_2 plasma without the bias voltage is shown as curve I in Figure 1a, revealing that the spectrum contains C_2 swan system

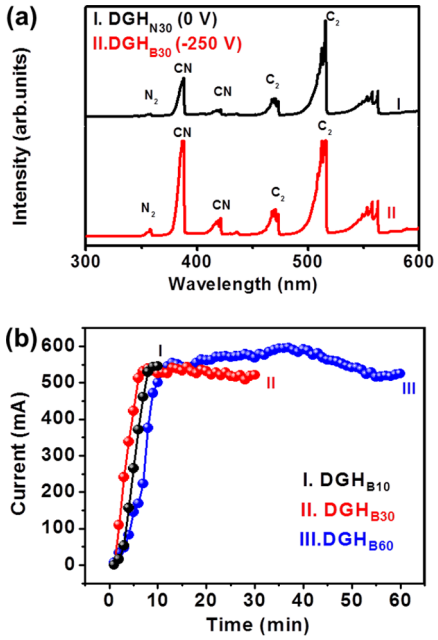

Figure 1. (a) The optical emission spectra of the CH_4(6%)/N_2 plasma (I) without the application of bias voltage and (II) under the application of −250 V bias voltage; (b) the evolution of bias current for the films grown in CH_4/N_2 plasma under −250 V bias for (I) 1, (II) 30, and (III) 60 min.

at ~468 nm and ~516 nm and CN peaks at ~386 nm and ~418 nm, respectively.[26] The C_2 and CN species are the main species that modify the microstructure of the BEG-DGH films. There are also small N_2 peak near ~358 nm and N-species in the 540−550 nm range, which are presumed to have less effect on modifying the granular structure of the films. Curve II in Figure 1a shows that the application of bias voltage increases the intensity of each OES peaks and notably increases the CN/C_2 peak ratio, implying that the reactivity of species in the plasma has increased markedly. Moreover, the bias current evaluation gives essential information for understanding the growth behavior of diamond films under bias voltages. Figure1b shows the evolution of bias current during the applied negative bias voltage for different growth times. The bias current increases abruptly at the instant of the application of bias

DOI: 10.1021/acsami.5b03166
ACS Appl. Mater. Interfaces 2015, 7, 14035−14042

voltage and reaches a saturated value (586 mA/cm^2) at around 5.6 min after the application of bias voltage, indicating that the diamond nuclei form instantaneously due to the application of bias voltage and fully cover the Si substrates rapidly. It should be noted that saturation current of CH_4/H_2 and CH_4/Ar plasma used for growing the MCD films[21] and UNCD films,[23] respectively, achieved only 58 and 270 mA/cm^2, implying that BEG DGH films possess larger EFE capacity than BEG MCD and BEG UNCD films.

Figure 2 shows SEM micrographs of the DGH films grown with and without applied bias at various growth times. From

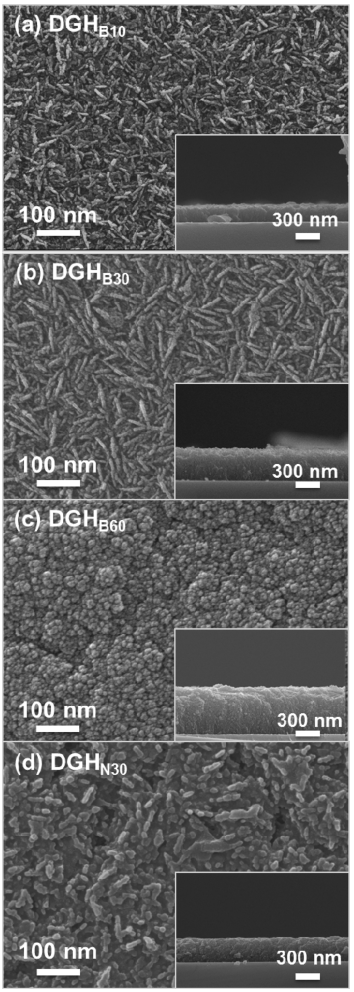

Figure 2. SEM micrographs for (a) DGH_{B10}, (b) DGH_{B30}, and (c) DGH_{B60} films grown under −250 V bias voltage in $CH_4(6\%)/N_2$ plasma and for (d) DGH_{N30} films grown without the bias voltage in $CH_4(6\%)/N_2$ plasma.

these micrographs, it is observed that there are noticeable changes in the morphology of the films with the growth time, when the films were grown under bias voltage. In Figure 2a, for DGH_{B10} films, there are small acicular diamond grains around 50 nm in length, whereas in Figure 2b, for DGH_{B30} films, the acicular grains grew longer, to around 100 nm. The granular structure changes markedly for the DGH_{B60} films. Figure 2c shows that these films contain equi-axed diamond grains of cauliflower-like geometry. In contrast, Figure 2d shows that the DGH_{N30} films contain rod-shaped diamond grains, which is totally different from those of the bias grown DGH_{BT} films. The granular structure of the DGH_{NT} films, which are grown biaslessly, insignificantly changes with the growth time (not shown). The thicknesses of the DGH films are estimated from the cross-sectional SEM micrographs of the films, which are shown as insets of each micrograph in Figure 2. The thickness of the film is ∼1028 nm for DGH_{BT60} films, resulting in an average growth rate of 17.0 nm/min for DGH_{BT} films grown under the application of bias voltage. On the other hand, the growth rate for the DGH_{NT} films grown without bias is about only ∼13.1 nm/min. This observation clearly demonstrates that BEG process encouraged high growth rate of the DGH films.

Figure 3 shows the visible-Raman spectra for DGH films. Curve I in this figure shows that the Raman spectrum of

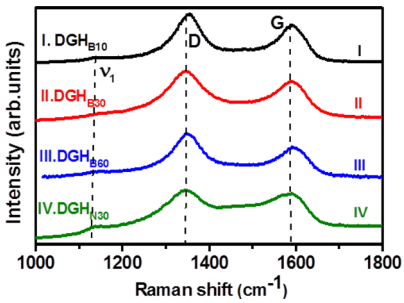

Figure 3. Raman spectra for (I) DGH_{B10}, (II) DGH_{B30} and (III) DGH_{B60} films grown under −250 V bias voltage in $CH_4(6\%)/N_2$ plasma and for (IV) DGH_{N30} films grown without the bias voltage in $CH_4(6\%)/N_2$ plasma.

DGH_{B10} films were predominated with D-band at 1350 cm^{-1} and G-band at 1580 cm^{-1}, which represents the disordered carbon and the graphitic phase, respectively.[27,28] There is a small peak at around 1120 cm^{-1} corresponding to the *trans*-polyacetylenephase.[29] The Raman spectroscopy is not markedly changed with the growth time, except that the D-band/G-band intensity ratio changed slightly (curves II and III, Figure 3), which is apparently due to the change in relative content of sp^3- to sp^2-bonded carbons in the films. However, the visible-Raman spectra are more sensitive to the sp^2-bonded carbon than the sp^3-bonded ones and therefore not possible to unambiguously analyze such a characteristic. A more appropriate analysis is EELS in TEM, which will be described later in this study. The Raman spectrum of DGH_{N30} films grown biaslessly (curve IV, Figure 3) is similar to those of DGH_{BT} films grown under bias voltage (cf. curves I−III, Figure 3).

3.2. Electrical Properties. The Hall measurement in van der Pauw configuration (ECOPIA, HMS-3000) reveals that the DGH_{BT} films grown under bias voltage are highly conductive. The electrical conductivity (σ) of DGH_{B10} films possesses a high value of σ_{B10} = 438 S/cm with electron concentration of $n_{B10} = 5.86 \times 10^{19}$ cm^{-3} and mobility of μ_{B10} = 63 cm^2/V·s. The conductivity of the films increased monotonously with growth time, reaching a high value of σ_{B60} = 1549 S/cm with electron concentration of $n_{B60} = 8.53 \times 10^{20}$ cm^{-3} and mobility of μ_{B60} = 279 cm^2/V·s for DGH_{B60} films. The conductivity of DGH_{BT} films are listed in Table 1, showing that it is markedly better than those of the DGH_{NT} films grown without bias voltage (σ_{N30} = 14.8 S/cm, $n_{N30} = 1.75 \times 10^{14}$ cm^{-3}, and μ_{N30} = 60 cm^2/V·s). Highly conducting characteristics of these films have led to excellent EFE properties.

Figure 4 shows the EFE properties of DGH films grown with and without bias voltage. The EFE characteristics are plotted as J_e versus E curves with the corresponding F−N plots shown as

DOI: 10.1021/acsami.5b03166
ACS Appl. Mater. Interfaces 2015, 7, 14035−14042

Table 1. Electrical Properties and Electron Field Emission Properties of DGH Films Grown in CH_4(6%)/N_2 Plasma under −250 V Applied Bias Voltage

	electrical properties			EFE properties			
samples	σ (S/cm)[a]	n_e (cm)$^{-3}$[a]	μ_e (cm^{-2}/V·s)[a]	E_0 (V/μm)[b]	J_e (mA/cm^2)[c]	β	τ (min)[d]
DGH_{B10}	438	5.86 × 10^{19}	63	4.5	2.2@8.2	1956	283
DGH_{B30}	900	9.35 × 10^{20}	103	2.9	3.8@6.0	2241	491
DGH_{B60}	1549	8.53 × 10^{20}	279	8.2	1.2@12.6	1404	147
DGH_{N30}	14.8	1.75 × 10^{14}	60	9.4	0.4@13.7	1252	

[a] σ, n_e, and μ_e: electrical conductivity, electron density, and mobility acquired from the Hall measurements using the van der Pauw configuration. [b] E_0: the turn-on field for EFE process that was designated as the point of interception of the straight lines extrapolated from the low and high-field segments of the F−N plots, namely, ln (J_e/E^2) versus 1/E plots. [c] J_e: the EFE current density evaluated at an applied field designated in parentheses. [d] τ: The lifetime of a microplasma device using these films as cathode measured at an applied voltage of 400 V.

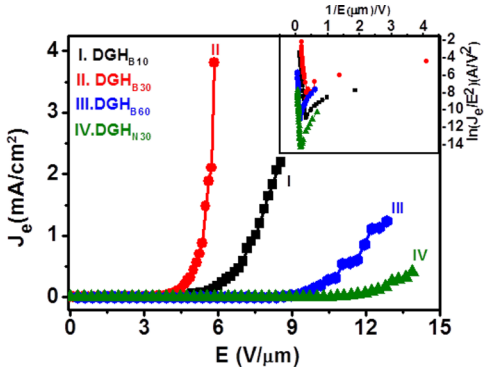

Figure 4. Electron field emission properties, J_e−E curves, for (I) DGH_{B10}, (II) DGH_{B30}, and (III) DGH_{B60} films grown under −250 V bias voltage in CH_4(6%)/N_2 plasma and for (IV) DGH_{N30} films grown without the bias voltage in CH_4(6%)/N_2 plasma. (Inset) Corresponding Fowler−Nordheim plots, that is, ln J_e/E^2 vs 1/E curves.

the insets. It is surprising to observe that for DGH_{BT} films grown under bias voltage, the EFE behavior changes markedly with the growth time. Curve I in Figure 4 shows that for DGH_{B10} films grown under bias for 10 min, the EFE process can be turned on at $(E_0)_{B10}$ = 4.5 V/μm, with EFE current density attaining a high value of $(J_e)_{B10}$ = 2.2 mA/cm^2 at E = 8.2 V/μm. The E_0 value reduces markedly to $(E_0)_{B30}$ = 2.9 V/μm, and the EFE current density increases to $(J_e)_{B30}$ = 3.8 mA/cm^2 at E = 6.0 V/μm for DGH_{B30} films. However, further increase in growth time (under bias) to 60 min changed the EFE behavior in reverse trend, resulting in $(E_0)_{B60}$ = 8.2 V/μm and $(J_e)_{B60}$ = 1.2 mA/cm^2 (at E = 12.6 V/μm) for DGH_{B60} films even though these films retain higher conductivity than the DGH_{B30} films. Nevertheless, all the DGH_{BT} films grown under bias voltage exhibit superior EFE properties to those of the DGH_{NT} films grown without bias voltage, that is, $(E_0)_{N30}$ = 9.4 V/μm and $(J_e)_{N30}$ = 0.4 mA/cm^2 (at E = 13.7 V/μm). The field enhancement factor (β) for these DGH films were evaluated from the slope of F−N plots, resulting in $(\beta)_{B10}$ = 1956, $(\beta)_{B30}$ = 2241, and $(\beta)_{B60}$ = 1404 for BT series of films grown under the bias voltage and is $(\beta)_{N30}$ = 1252 for the films grown biaslessly.

To evaluate the robustness of the DGH_{BT} films, we utilized these materials as cathodes for microplasma devices, as the cathode materials in these devices are subjected to continuous bombardment of energetic Ar-ions which is considered as the harshest environment in device applications. Figure 5 shows the sequence of PI images of the DGH_{BT}-based microplasma devices ignited at 2 Torr, where the ignition of the plasma is designated as the threshold breakdown voltage (V_{th}). These PI images show that the devices using DGH_{B30} films as cathodes (panel II, Figure 5) exhibit superior illumination behavior to those using DGH_{B10} (panel I, Figure 5) and DGH_{B60} (panel III, Figure 5) as cathodes. The microplasma devices using the DGH_{B30} films as the cathode can be triggered by a voltage as low as 320 V(panel II, Figure 5), whereas those using DGH_{B10} and DGH_{B60} as cathode need higher voltage to trigger the plasma, that is, around 370 V for the former and 430 V for the latter. The intensity of the PI behavior increases monotonically

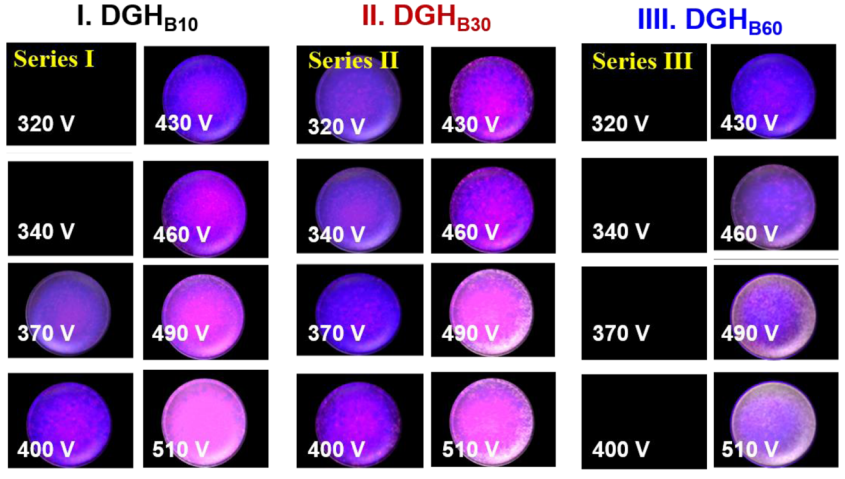

Figure 5. Plasma illumination images of microplasma devices using (I) DGH_{B10}, (II) DGH_{B30}, and (III) DGH_{B60} films grown under −250 V bias voltage in CH_4(6%)/N_2 plasma as cathode.

DOI: 10.1021/acsami.5b03166
ACS Appl. Mater. Interfaces 2015, 7, 14035−14042

with the applied voltage. The PI characteristics of the microplasma devices are better illustrated by the variation of the plasma current density (J_{pl}) versus the applied voltage (V) curves, which is plotted in Figure 6a. The plasma density (n_e)

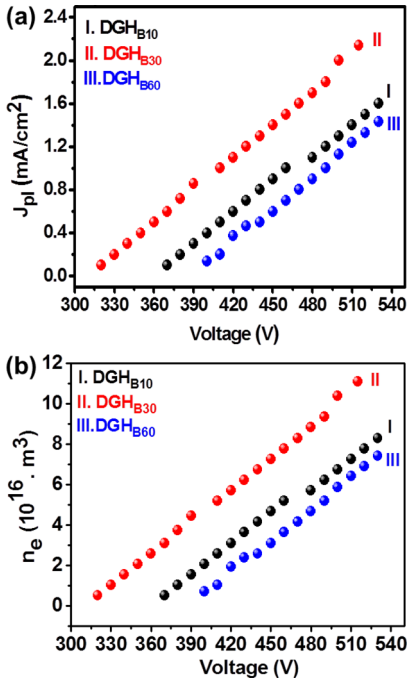

Figure 6. (a) Plasma current density versus applied voltage (J_{pl}–V) and (b) plasma density versus applied voltage (n_e–V) characteristics of microplasma devices using (I) DGH_{B10}, (II) DGH_{B30}, and (III) DGH_{B60} films grown under −250 V bias voltage in $CH_4(6\%)/N_2$ plasma as cathode.

for the microplama devices, which is also the number density of the electrons in the plasma can be calculated from the J_{pl} values using modified Child's law.[30,31] The plasma density (n_e) versus the applied voltage (V) curves is plotted in Figure 6b. Generally, J_{pl} and n_e increase with the applied field voltage. Curve II in Figure 6a shows that, for DGH_{B30} based microplasma device, the J_{pl} value increases monotonically with the applied voltage from 0.09 mA/cm^2 at V_{th} = 320 V reaching a J_{pl} value of 2.14 mA cm^{-2} at an applied voltage of 515 V. Correspondingly, curve II in Figure 6b shows that the n_e value increases from 0.6 × 10^{16} cm^{-3} at $(V_{th})_{PI}$ = 320 V monotonously with the applied voltage, reaching a n_e value of 1.12 × 10^{17} cm^{-3} at an applied voltage of 515 V. These J_{pl} (or n_e) values are higher than those for DGH_{B10} (or DGH_{B60}) based microplasma devices (curves I and III of Figure 6). It is interesting to observe that the microplasma devices, which used the materials with the best EFE properties rather than the highest conductivity as cathode exhibits the highest J_{pl} (or n_e) values.

Device stability is an important parameter for practical applications. The lifetime stability of the DGH-based microplasma devices were examined over an extensive period with a constant applied voltage of 450 V and the results are shown in Figure 7. The PI behavior of the DGH_{B30}-based microplasma devices remains stable over 491 min (8.16 h) with the plasma current of 130 μA, showing the highest stability (curve II, Figure. 7). In contrast, DGH_{B10}-based devices sustain only 283 min (4.71 h) with plasma current of 110 μA (curve I, Figure. 7)

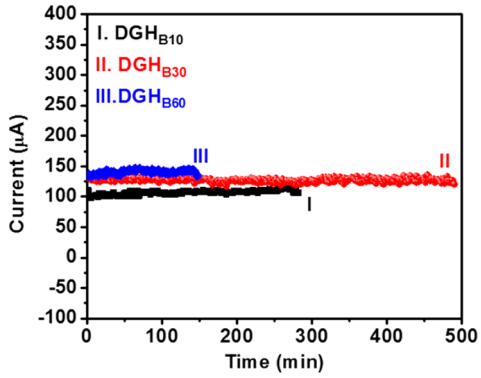

Figure 7. Lifetime measurements under applied voltage of 450 V for microplasma devices using (I) DGH_{B10} films, (II) DGH_{B30} films and (III) DGH_{B60} films, which were grown under −250 V bias voltage in $CH_4(6\%)/N_2$ plasma, as cathode.

and DGH_{B60}-based ones sustain 147 min (2.45 h) with plasma current of 101 μA (curve III, Figure 7). The DGH_{B30}-based microplasma devices possess the highest lifetime stability as well as the best plasma illumination properties (i.e., higher plasma density, n_e), compared with those of DGH_{B10} and DGH_{B60}-based ones, which can be closely correlated with the superior EFE properties of the DGH_{B30} cathode materials. Notably, the higher conductivity of the DGH_{B60} materials does not lead to better plasma illumination behavior and longer lifetime for the corresponding microplasma devices. It seems that the better the EFE behavior of the cathode materials, the better the PI properties of the microplasma devices.

3.3. Microstructural Evolution of DGH_{BT} Films.

Apparently, the improved electrical conductivity and EFE properties of DGH_{BT} films are closely related to the microstructure of the films. To understand how these characteristics are correlated, we investigated the microstructures of the DGH_{BT} films using TEM. The bright field (BF) TEM micrographs of DGH_{B10} shown in Figure 8a$_I$ indicate that these films consist of diamond grains with dendrite-like geometry. Selective area electron diffraction (SAED) pattern shown in the inset of Figure 8a$_I$ reveals a typical ring pattern corresponding to the $(111)_D$, $(220)_D$, and $(311)_D$ lattice planes of diamond, confirming that the films are predominately diamond. A diffuse ring appears in the center of SAED, implying the existence of a-C in these materials. The size distribution of diamond grains in the DGH_{B10} films is better illustrated by the composed dark field (c-DF) image in Figure 8a$_{II}$, which is the superposition of several dark field images acquired using different diffraction spots (yellow and green circles, inset in Figure 8a$_{II}$). The c-DF image in Figure 8a$_{II}$ reveals that the films contain some graphite (green) with diamond grains (yellow) as majority phase.

Figure 8b$_I$b$_{II}$ shows the BF and c-DF TEM micrographs of DGH_{B30} films, which reveal that these films contain very unique granular structure. They consist of needle-like diamond grains of the size around 5 nm in diameter and hundreds of nanometers in length. The SAED pattern also contains $(111)_D$, $(220)_D$, and $(311)_D$ rings of diamond material and a central diffuse ring of a-C phase. In addition, this SAED contains an extra thick ring of smaller diameter than the $(111)_D$ ring that corresponds to (0001) lattice of graphite materials (indicated by the arrow in the inset of Figure 8b$_I$). The presence of $(0001)_g$ ring implies the existence of abundant randomly oriented nanographite clusters. The c-DF image in Figure 8b$_{II}$

DOI: 10.1021/acsami.5b03166
ACS Appl. Mater. Interfaces 2015, 7, 14035−14042

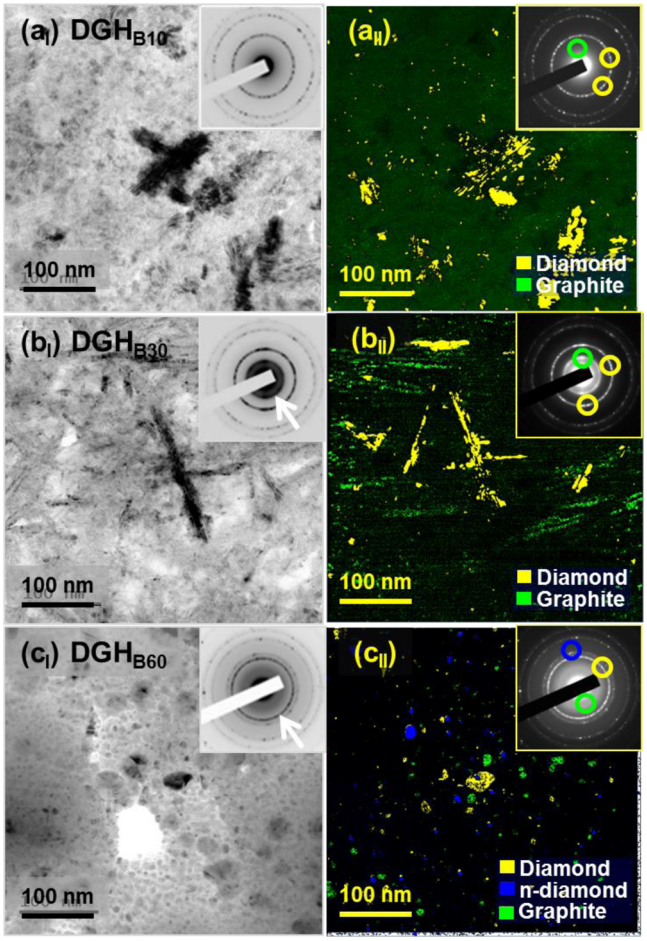

Figure 8. (a_I, b_I, and c_I) Bright field (BF) and (a_{II}, b_{II}, and c_{II}) composed dard field (c-DF) TEM micrographs for (a_I and a_{II}) DGH_{B10}, (b_I and b_{II}) DGH_{B30}, and (c_I and c_{II}) DGH_{B60} films grown under −250 V bias voltage in $CH_4(6\%)/N_2$ plasma.

reveals that each of the needle-like diamond grains (yellow) is sandwiched between the graphitic phases (green). On the other hand, Figure 8c_I,c_{II} shows the BF and DF TEM micrographs of DGH_{B60} films. The needle-like granular structure of the diamond grains is no longer observable. Instead, a large number of equi-axed aggregates appears around 20−30 nm in size in addition to the ultrasmall diamond grains. The SAED shown in the inset of Figure 8c_I reveals that the diamond rings, $(111)_D$, $(220)_D$, and $(311)_D$ are much weaker in intensity. There exists an extra ring with smaller size than the $(111)_D$ ring (indicated by the arrow in the inset of Figure 8c_I), which corresponds to n-diamond, an allotropy of diamond with FCC structure (diamond is of Fd3m structure). Moreover, a large diffuse ring appears in the center of SAED, revealing the presence of large proportion of sp^2-bonded carbon. Again, the phase constituents of the films are more clearly illustrated in c-DF image (Figure 8c_{II}).

The bonding structures of the samples were examined using EELS in TEM. Notably, while core-loss EELS spectrum shows the general feature of the diamond as σ^*-band and the graphite (or a-C carbon) as π^*-band, it is plasmon-loss EELS spectrum, which can unambiguously differentiate the a-C and the graphite phase in sp^2-bonded carbon. In the plasmon-loss EELS spectrum, a-C shows a peak near 22 eV (ω_{d1}-band), whereas the crystalline ones show a peak near 27 eV (ω_{d3}-band).[32−35] In contrast, the diamond phase exhibits a peak at 33 eV (ω_{d2}-band) corresponding to bulk plasmon with a shoulder at 23 eV (ω_{d2}-band) corresponding to surface plasmon with ω_{d2}/ω_{d4} peak ratio $\sim 1/\sqrt{2}$.[32−35] Figure 9 shows the selected area core-loss and plasmon-loss EELS spectra of the DGH_{BT} films. Curve II in Figure 9a shows an abrupt rise near 289.5 eV(σ^*-band) and a large dip in the vicinity of 302.0 eV for DGH_{B30} films, which clearly indicates the diamond nature of these materials.[32−35] A weak peak at 285.2 eV (π^*-band) in the curves signifies a small fraction of sp^2-bonded phase present in these films. Moreover, curve II in Figure 9b reveals clearly the presence of ω_{d2}- and ω_{d4}-bands in the plasmon-loss EELS of DGH_{B30} films, indicating, that these films are predominately diamond. The core-loss EELS for DGH_{B10} films shown in curve I of Figure 9a also contains a σ^*-band at 289.5 eV and a deep valley in the vicinity of 302.0 eV, which signifies that these films are also predominately diamond. The peak intensity at 285.2 eV in curve I is markedly smaller, implying the decrease in graphitic sp^2-bonded carbon present in these films. However, ω_{d2} and ω_{d4}-bands cannot be distinctly differentiated in curve I in Figure 9b for DGH_{B10} films because these films contain large proportion of Si signal that distorted the plasmon-loss EELS markedly, and the signature of diamond cannot be clearly resolved. The presence of Si signal is presumably owing to the small thickness of the films. On the other hand, the core-loss EELS of DGH_{B60} films (curve III, Figure 9a) completely lose the signature of diamond, implying the disappearance of diamond phase and the presence of large proportion of sp^2-bonded phase in these films. The plasmon-loss EELS shown in curve III in Figure 9b corresponding to DGH_{B60} films shows only one large peak near 26.4 eV, which is apparently the combination of ω_{d3}-band at 27 eV and ω_{d1}-band at 22 eV with very small percentage of $\omega_{d2}+\omega_{d4}$-band, that is, these materials

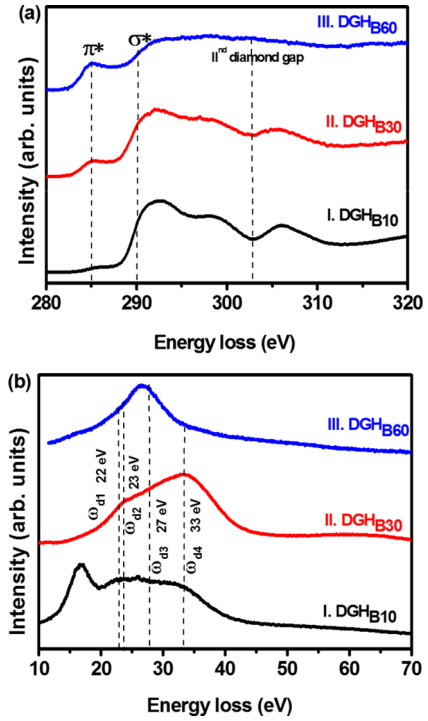

Figure 9. Selected area (a) core-loss and (b) plasmon-loss EELS for (I) DGH_{B10}, (II) DGH_{B30}, and (III) DGH_{B60} films grown under −250 V bias voltage in $CH_4(6\%)/N_2$ plasma.

DOI: 10.1021/acsami.5b03166
ACS Appl. Mater. Interfaces 2015, 7, 14035−14042

contain mainly graphite phase with very small proportion of diamond phase. The observations in EELS spectroscopy is in accord with the TEM microstructure shown in Figure 8.

4. DISCUSSION

It should be mentioned that in the preparation of TEM foil, the samples were ion-milled from the Si-sides such that the TEM foil mainly contains the materials near the surface region of the films. Therefore, the TEM micrographs shown in Figure 8 represent the microstructure of the surface layer of DGH_{BT} films grown for different durations of time. These micrographs also reflect the microstructure of the materials located at different depths of a thicker film such as DGH_{B60}. That is, Figure 8 also represents how the microstructure of the films evolves while the films grow thicker. The growth of diamond films starts with the formation of a-C on Si surface prior to the presence of diamond nuclei.[36] Abundant spherical diamond clusters were nucleated due to the abundance of C_2-species in the CH_4/N_2 plasma.[19] The application of −250 V bias voltage markedly increased the kinetic energy of the C_2^+ species that further enhanced the nucleation rate of diamond clusters.[21] However, there is also a large proportion of CN-species present in the plasma (cf. Figure 1a), which tends to adhere onto the $(0\bar{2}2)$ surface of the diamond clusters,[19] enhancing the growth of diamond along the $0\bar{2}2$ direction, and resulted in rod-shaped diamond grains. As the nanosized diamond rods grow longer, they entangle one another, resulting in a dendrite-like granular structure, like the one shown in Figure 8a. The diamond grains became thinner as they grew longer and finally formed needle-like diamond grains, as shown in Figure 8b. Notably, in this region, every needle-like diamond grain is encapsulated with a graphene-like phase a few layers thick. The presence of the graphene-like layer hindered the formation of diamond bonds, resulting in the formation of incompletely crystallized diamond, such as n-diamond with equi-axed granular structure, such as the one shown in Figure 8c. The needle-like diamond grains are no more observable. The presence of −250 V bias voltage accelerated the anisotropic growth of rod-shaped diamond grains due to the increased CN/C_2 ratio (cf. Figure 1a) which, in turn, results in rapid transition of microstructure from dendrite-like to needle-like and, finally, to equi-axed granular structure. Therefore, for a thick film such as DGH_{B60} films, there exist three layers, each with a different microstructure. As schematically illustrated in Figure10, after the formation of a thin a-C, the first layer of dendrite-like diamond forms (region I), followed by the sequential formation of needle-like diamond (region II) and a layer of equi-axed granular structured materials, which mainly consist of n-diamond and graphitic phase with diamond as minor phase (region III).

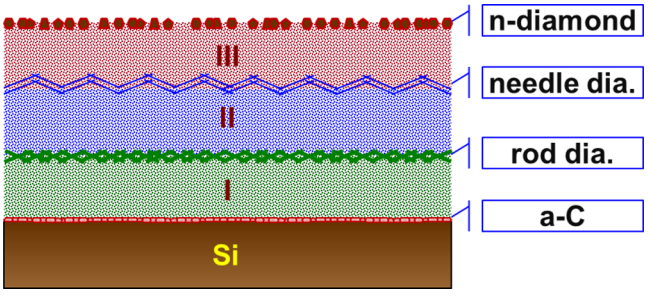

Figure 10. Schematic diagram shows the evolution of microstructure as the diamond films grew with time in $CH_4(6\%)/N_2$ plasma under applied voltage of −250 V: the a-C layer formed first, followed by the formation of diamond grains with (I) short-rod geometry and (II) needle-like geometry, sequentially, and, finally, (III) a layer predominated with the n-diamond clusters.

Interestingly, by controlling the growth time, we can manipulate the microstructure of the surface. The films with granular structure, like the one shown in Figure 8b, exhibits the best EFE properties, whereas the films with the microstructure similar to Figure 8c possess highest conductivity but do not have good EFE properties (cf. Table 1). The implication of these results is that high conductivity by itself does not guaranty good EFE properties. This is presumably due to the fact that for the DGH_{B60} films (cf. Figure8c), the emission sites are mostly nanographite clusters or defective diamond cluster (n-diamond clusters), which are not appropriate emitting sites. Apparently, the most favorable geometry for the emission sites are nanosized diamond grains with needle-like geometry, especially when they are encased with graphene-like layers. These encapsulating layers can transport electrons efficiently to the diamond for field emitting sites. Therefore, the microstructure similar to Figure 8b exhibits the best EFE properties (cf. Table 1).

5. CONCLUSIONS

DGH films were bias enhanced grown with different growth times in CH_4/N_2 plasma. The changes in the morphology/microstructure in the films due to the difference in growth time under the application of bias voltage was studied in detail by SEM, Raman spectroscopy, and TEM. TEM investigation reveals that the application of bias voltage stimulated the transformation of microstructure while the films grew thicker. The most favorable granular structure for EFE application is the existence of nanographite phases surrounding the needle-like diamond grain as in DGH_{B30} films, such that the electrons can be transported easily along the graphite phases to the emitting surface. These films possess the lowest turn-on field of 2.9 V/μm and the highest EFE current density of 3.8 mA/cm^2 at an applied field of 6.0 V/μm. Extending the growth time to 60 min converts the needle-like diamond grains into equi-axed n-diamond cluster along with abundant nanographite clusters that gives even better electrical conductivity but results in degraded EFE properties. These observations make clear that the conductivity and EFE properties of the materials can be tailored over a wide range that may open up a pathway for the advanced high-definition flat panel displays and microplasma device applications.

AUTHOR INFORMATION

Corresponding Author

*E-mail: inanlin@mail.tku.edu.tw.

Notes

The authors declare no competing financial interest.

ACKNOWLEDGMENTS

The authors would like to thank the Ministry of Science and Technology, Republic of China, for financial support through project No. MOST 103-2112-M-032-002.

REFERENCES

(1) Geis, M. W.; Deneault, S.; Krohn, K. E.; Marchant, M.; Lyszczarz, T. M.; Cooke, D. L. Field Emission at 10 V cm^{-1} with Surface

DOI: 10.1021/acsami.5b03166
ACS Appl. Mater. Interfaces 2015, 7, 14035−14042

Emission Cathodes on Negative-electron-affinity Insulator. *Appl. Phys. Lett.* **2005**, *87*, 192115.
(2) Hojati-Talemi, P.; Simon, G. P. Field Emission Study of Graphene Nanowalls Prepared by Microwave-Plasma Method. *Carbon* **2011**, *49*, 2869−2877.
(3) Itoh, T.; Shimabukuro, S.; Kawamura, S.; Nonomura, S. Preparation and Electron Field Emission of Carbon Nanowall by Cat-CVD. *Thin Solid Films* **2006**, *501*, 314−317.
(4) Kohn, E.; Adamschik, M.; Schmid, P.; Ertl, S.; Floter, A. Diamond Electromechanical Micro Devices—Technology and Performance. *Diamond Relat. Mater.* **2001**, *10*, 1684−1691.
(5) Zhu, W.; Kochanski, G. P.; Jin, S. Low-Field Electron Emission fromUndoped Nanostructured Diamond. *Science* **1998**, *282*, 1471−1473.
(6) Kang, W. P.; Davidson, J. L.; Wisitsoraat, A.; Kerns, D. V.; Kerns, S. Recent Development of Diamond Microtip Field Emitter Cathodes and Devices. *J. Vac. Sci. Technol.* **2001**, *19*, 936−941.
(7) Geis, M. W.; Efremow, N. N.; Krohn, K. E.; Twichell, J. C.; Lszczarz, T. M.; Kalish, R.; Greer, J. A.; Tabat, M. D. A New Surface Electron-Emission Mechanism in Diamond Cathodes. *Nature* **1998**, *393*, 431−435.
(8) Ikeda, T.; Teii, K. Origin of Low Threshold Field Emission from Nitrogen-Incorporated NanocrystallineDiamond Films. *Appl. Phys. Lett.* **2009**, *94*, 143102.
(9) Sowers, A. T.; Ward, B. L.; English, S. L.; Nemanich, R. J. Field Emission Properties of Nitrogen-Doped Diamond Film. *J. Appl. Phys.* **1999**, *86*, 3973−3982.
(10) Zhou, D.; Krauss, A. R.; Qin, L. C.; McCauley, T. G.; Gruen, D. M.; Corrigan, T. D.; Chang, R. P. H.; Gnaser, H. Synthesis and Electron Field Emission of Nanocrystalline Diamond Thin Films Grown from N_2/CH_4 Microwave Plasmas. *J. Appl. Phys.* **1997**, *82*, 4546−4550.
(11) Krauss, A. R.; Auciello, O.; Ding, M. Q.; Gruen, D. M.; Huang, Y.; Zhirnov, V. V.; Givargizov, E. I.; Breskin, A.; Chechen, R.; Shefer, E.; Konov, V.; Pimenov, S.; Karabutov, A.; Rakhimov, A.; Suetin, N. Electron Field Emission for Ultrananocrystalline Diamond Films. *J. Appl. Phys.* **2001**, *89*, 2958−2967.
(12) Corrigan, T. D.; Krauss, A. R.; Gruen, D. M.; Auciello, O.; Chang, R. P. H. Low Temperature Growth of Nanocrystalline Diamond Films on Glass Substrates for Field Emission Applications. *Mater. Res. Soc. Symp. Proc.* **2000**, *593*, 233−236.
(13) Sankaran, K. J.; Kumar, N.; Kurian, J.; Ramadoss, R.; Chen, H. C.; Tyagi, A. K.; Dash, S.; Lee, C. Y.; Tai, N. H.; Lin, I. N. Improvement in Tribological Properties by Modification of Grain Boundary and Microstructure of Ultrananocrystalline Diamond Films. *ACS Appl. Mater. Interfaces* **2013**, *5*, 3614−3624.
(14) Krauss, A. R.; Gruen, D. M.; Zhou, D.; McCauley, T. G.; Qin, L. C.; Corrigan, T. D.; Auciello, O.; Chang, R. P. H. Morphology and Electron Emission Properties of Nanocrystalline CVD Diamond Thin Films. *Mater. Res. Soc. Symp. Proc.* **1998**, *495*, 299−310.
(15) Birrell, J.; Carlisle, J. A.; Auciello, O.; Gruen, D. M.; Gibson, J. M. Morphology and Electronic Structure in Nitrogen-Doped Ultrananocrystalline Diamond. *Appl. Phys. Lett.* **2002**, *81*, 2235.
(16) Williams, O. A.; Curat, S.; Gerbi, J. E.; Gruen, D. M.; Jackman, R. B. *n*-Type Conductivity in Ultrananocrystalline Diamond Films. *Appl. Phys. Lett.* **2004**, *85*, 1680.
(17) Arenal, R.; Bruno, P.; Miller, D. J.; Bleuel, M.; Lal, J.; Gruen, D. M. Diamond Nanowires and the Insulator-Metal Transition in Ultrananocrystalline Diamond Films. *Phys. Rev. B* **2007**, *75*, 195431.
(18) Lin, Y. C.; Sankaran, K. J.; Chen, Y. C.; Lee, C. Y.; Chen, H. C.; Lin, I. N.; Tai, N. H. Enhancing Electron Field Emission Properties of UNCD films Through Nitrogen Incorporation at High Substrate Temperature. *Diamond Relat. Mater.* **2011**, *20*, 191−195.
(19) Sankaran, K. J.; Kurian, J.; Chen, H. C.; Dong, C. L.; Lee, C. Y.; Tai, N. H.; Lin, I. N. Origin of a Needle-like Granular Structure for Ultrananocrystalline Diamond Films Grown in a N_2/CH_4 Plasma. *J. Phys. D: Appl. Phys.* **2012**, *45*, 365303.
(20) Panda, K.; Sankaran, K. J.; Panigrahi, B. K.; Tai, N. H.; Lin, I. N. Direct Observation and Mechanism for Enhanced Electron Emission in Hydrogen Plasma-Treated Diamond Nanowire Films. *ACS Appl. Mater. Interfaces* **2014**, *6*, 8531−8541.
(21) Teng, K. Y.; Chen, H. C.; Tzeng, G. C.; Tang, C. Y.; Cheng, H. F.; Lin, I. N. Bias-Enhanced Nucleation and Growth Processes for Improving the Electron Field Emission Properties of Diamond Films. *J. Appl. Phys.* **2012**, *111*, 053701.
(22) Saravanan, A.; Huang, B. R.; Sankaran, K. J.; Keiser, G.; Kurian, J.; Tai, N. H.; Lin, I. N. Structural Modification of Nano-crystallineDiamond Films via Positive/Negative Bias Enhanced Nucleation and Growth Processes for Improving Their Electron Field Emission Properties. *J. Appl. Phys.* **2015**, *117*, 215307.
(23) Saravanan, A.; Huang, B. R.; Sankaran, K. J.; Kunuku, S.; Dong, C. L.; Leou, K. C.; Tai, N. H.; Lin, I. N. Bias-Enhanced Nucleation and Growth Processes for Ultrananocrystalline Diamond Films in Ar/CH_4 Plasma and Their Enhanced Plasma Illumination Properties. *ACS Appl. Mater. Interfaces* **2014**, *6*, 10566−10575.
(24) Lee, Y. C.; Lin, S. J.; Lin, C. Y.; Yip, M. C.; Fang, W.; Lin, I. N. Pre-Nucleation Techniques for Enhancing Nucleation Density and Adhesion of Low Temperature Deposited Ultra-Nanocrystalline Diamond. *Diamond Relat. Mater.* **2006**, *15*, 2046−2050.
(25) Fowler, R. H.; Nordheim, L. Electron Emission in Intense Electric Fields. *Proc. R. Soc. London, Ser. A* **1928**, *119*, 173−181.
(26) Wang, C. S.; Tong, G. H.; Chen, H. C.; Shih, W. C.; Lin, I. N. Effect of N_2 Addition in ArPlasma on the Development of Microstructure of Ultra-nanocrystalline Diamond Films. *Diamond Relat. Mater.* **2010**, *19*, 147−152.
(27) Ferrari, A. C.; Robertson, J. Origin of the 1150 cm^{-1} Raman Mode in Nanocrystalline Diamond. *Phys. Rev. B* **2001**, *63*, 121405.
(28) Chen, Q.; Gruen, D. M.; Krauss, A. R.; Corrigan, T. D.; Witek, M.; Swain, G. M. J. The Structure and Electrochemical Behavior of Nitrogen- Containing Nanocrystalline Diamond Films Deposited from $CH_4/N_2/Ar$ Mixtures. *Electrochem.Soc.* **2001**, *148*, 44−41.
(29) Kuzmany, H.; Pfeiffer, R.; Salk, N.; Günther, B. The Mystery of the 1140 cm^{-1} Raman Line in Nanocrystalline Diamond Films. *Carbon* **2004**, *42*, 911−917.
(30) Lieberman, M. A.; Lichtenberg, A. J. *Principle of Plasma Discharges and Materials Processing*; John Wiley & Sons: Hoboken, NJ, 2005, 2nd ed.
(31) Chapman, B. *Glow Discharge Processes, Sputtering and Plasma Etching*; John Wiley & Sons, New York, 1980.
(32) Kovarik, P.; Bourdon, E. B. D.; Prince, R. H. Electron Energy Loss Characterization of Laser-Deposited *a*-C, *a*-C:H and Diamond Films. *Phys. Rev. B* **1993**, *48*, 12123.
(33) Prawer, S.; Peng, J. L.; Orwa, J. O.; McCallum, J. C.; Jamieson, D. N.; Bursill, L. A. Size Dependence of Structural Stability in Nanocrystalline Diamond. *Phys. Rev. B* **2000**, *62*, R16360.
(34) Chen, S. S.; Chen, H. C.; Wang, W. C.; Lee, C. Y.; Lin, I. N. Effects of High Energy Au-Ion Irradiation on the Microstructure of Diamond Films. *J. Appl. Phys.* **2013**, *113*, 113704.
(35) Kurian, Joji.; Sankaran, K. J.; Thomas, J. P.; Tai, N. H.; Chen, H. C.; Lin, I. N. The Role of Nanographitic Phase on Enhancing the Electron Field Emission Properties of Hybrid Granular Structured Diamond Films: The Electron Energy Loss Spectroscopic Studies. *J. Phys. D: Appl. Phys.* **2014**, *47*, 415303.
(36) Chang, T. H.; Panda, K.; Panigrahi, B. K.; Lou, S. C.; Chen, C.; Chan, H. C.; Lin, I. N.; Tai, N. H. Electrophoresis of Nanodiamond on the Growth of Ultrananocrystalline Diamond Films on Silicon Nanowires and the Enhancement of the Electron Field Emission Properties. *J. Phys. Chem. C* **2012**, *116*, 19867−19876.

DOI: 10.1021/acsami.5b03166
ACS Appl. Mater. Interfaces 2015, 7, 14035−14042